

Cite this: *Chem. Sci.*, 2025, 16, 7339

All publication charges for this article have been paid for by the Royal Society of Chemistry

# Isorecticular 3D covalent organic frameworks with non-interpenetrated pcu-derived dia topology: pore regulation from micropores to mesopores†

Xilin Li, Tongyi Zhao, Fengzhen Wang, Wenxuan Wu, Yali Sun, Hao Ren  and Fuxing Sun \*

Three-dimensional (3D) covalent organic frameworks (COFs) offer tremendous potential for a range of applications due to their unique structural and porous features. However, achieving the reticular synthesis of 3D COFs with regulated pores through isorecticular expansion remains a significant challenge, primarily due to the occurrence of interpenetration. In this study, we present a novel strategy that utilizes high-coordinated building blocks, acting as a binodal group of tetrahedral nodes, to synthesize isorecticular 3D COFs (JUC-300 to -302) with tunable pore sizes and uncommon non-interpenetrated pcu-derived dia topology. The pore sizes of these COFs were successfully tuned from 1.6 to 5.2 nm. The mesopores with a size of 5.2 nm in JUC-302 are the largest reported among 3D COFs to date and demonstrated the effective incorporation of a large protein, myoglobin. The strategy provides a new pathway for synthesizing isorecticular 3D COFs with reduced interpenetration, enabling applications that depend on various pore sizes.

Received 17th February 2025

Accepted 17th March 2025

DOI: 10.1039/d5sc01227a

rsc.li/chemical-science

## Introduction

Covalent organic frameworks (COFs) are a remarkable class of porous materials that could be created by designing linking organic building units based on reticular chemistry.<sup>1,2</sup> These materials usually exhibit good crystallinity and tunable pores and have widespread potential for various applications, including gas storage and separation,<sup>3,4</sup> catalysis,<sup>5,6</sup> sensing,<sup>7</sup> etc.<sup>8</sup> Over the past decade, most efforts in new COFs have been devoted to two-dimensional (2D) COFs, which are laminar structures.<sup>9</sup> Three-dimensional (3D) COFs have recently received attention owing to their high structural diversity, complicated pore morphology, and increased pore accessibility, offering an expansive platform for tuning their pore features and functions.<sup>10,11</sup> However, there are several obstacles in the pursuit of designing and synthesizing new 3D COFs: the few available geometry-specific organic monomers as building blocks,<sup>12–14</sup> the challenge in determining their accurate structures,<sup>15,16</sup> and the difficulties in expanding their topological structures and tuning their pore apertures based on reticular chemistry.<sup>17</sup>

One fundamental challenge and advantage in the reticular synthesis<sup>18</sup> of crystalline porous frameworks including metal-organic frameworks (MOFs) and COFs is to alter their

composition, functionality, and pore dimensions systematically.<sup>19,20</sup> The tunable pore size of isorecticular porous frameworks could be suitable for adsorption-based applications for different kinds of molecules. In particular, large pores above 2 nm are scarce and highly desirable in crystalline porous materials, which are useful for the inclusion of large guests such as dyes, biomolecules, etc.<sup>21</sup> However, when researchers attempt to alter their pore sizes through isorecticular expansion, which involves elongating the linkers without changing the underlying topology and is considered the most effective method in reticular chemistry, interpenetration often occurs for three-dimensional (3D) frameworks.<sup>22,23</sup> The interpenetration generally restricts the pore size, although it can also enhance the robustness of the framework.<sup>24</sup>

To suppress interpenetration and obtain large pores, several strategies have been developed in MOF synthesis, such as control of reaction conditions, use of templates, steric hindrance of ligands, etc.<sup>25,26</sup> However, the applications of these strategies for COFs are relatively rare. A limited number of studies have demonstrated the interpenetration isomerism of 3D COFs through precise control of reaction conditions.<sup>27–29</sup> Additionally, a few studies have reported the strategy of steric hindrance utilized in the synthesis of 3D COFs to suppress interpenetration and achieve large pores.<sup>30–33</sup> Despite these efforts, the limitation of these strategies makes them generally ineffective for expanding pore size through isorecticular expansion. Another key approach to tune and push forward the pore sizes through isorecticular expansion and to reduce the interpenetrating degree is the precise choice of the target

State Key Laboratory of Inorganic Synthesis and Preparative Chemistry, Jilin University, Changchun, China. E-mail: fxsun@jlu.edu.cn

† Electronic supplementary information (ESI) available. See DOI: <https://doi.org/10.1039/d5sc01227a>



framework's topology. Generally, frameworks with one-dimensional (1D) pores are less prone to interpenetration. This strategy is highly effective for achieving pore regulation and large pore size, as seen in MOFs constructed from rod-shaped secondary building units<sup>34</sup> and 2D COFs.<sup>35</sup> For instance, Li *et al.* reported the isoreticular series of 2D COFs with **kgd** topology with pore sizes tuned from 0.67 to 1.2 nm.<sup>36</sup> The largest pore in COFs to date was also achieved by the isoreticular expansion of 2D COFs which are TD-COF-1 to 3 with **hcb** topology and the record pore sizes ranged from 7.7 to 10.0 nm.<sup>37</sup> 3D frameworks with cage-like nets can reduce the interpenetrating degree effectively. Isoreticular MOFs with tunable and ultra-large pores synthesized using this strategy are not uncommon.<sup>19,38–40</sup> By precisely selecting topologies with 1D pores or cages, 3D COFs with large pores can also be achieved,<sup>41</sup> such as **stp** COFs like JUC-564,<sup>42</sup> Trip-COF-1 and -2,<sup>43</sup> HFPTTAE and HFPTT-DMeTAB,<sup>44</sup> and TUS-64 (ref. 45) with pore sizes ranging from 2.9 to 4.4 nm and **bor** COFs like DBA-3D-COF<sup>46</sup> and 3D-bor-COF-1, -2 and -3 (ref. 47) with pore sizes from 2.8 to 3.8 nm. Recently, RICE-3 with **pto** topology was reported, and its pores reached 4.6 nm which is the record for 3D COFs so far.<sup>48</sup>

Despite these advancements, such studies are still limited due to the scarcity of suitable and available topologies and building blocks. What's more, the pore regulation and synthesis of isoreticular 3D COFs are even more difficult and infrequently reported.<sup>47,49–51</sup> In this work, we focused on the synthesis and pore-size tuning of isoreticular 3D COFs with **dia** topology. Our strategy involves designing high-coordinated building blocks that can be regarded as multi-nodal units, thus enabling the desymmetrization of targeted underlying nets and yielding distorted nets for isoreticular expansion to tune their pore sizes through reducing or even avoiding interpenetration. Using this strategy, we synthesized three isoreticular 3D COFs, named JUC-300 to -302 (JUC = Jilin University, China) with uncommon non-interpenetrated **pcu**-derived **dia** topology. The pore sizes of JUC-300 to -302 were successfully tuned from 1.6 to 5.2 nm. It is worth mentioning that the mesopore with a size of 5.2 nm in JUC-302 is larger than those in all other 3D COFs reported so far. Thanks to the large apertures, JUC-302 demonstrated favorable adsorption capacity of a large protein with suitable dimensions.

## Results and discussion

### Structural design

Among only about 30 topologies reported in 3D COFs up to now, **dia** topology is the most classical and widely studied. It is well known that the **dia** net is the underlying net of tetrahedral nodes with only one kind of edge (edge-transitive). It exhibits high-symmetry and uniform pore features. To create a 3D COF with **dia** topology, there are two routes in reported studies so far (Fig. 1a and b). The first and most common way is the utilization of monomers with tetrahedral shapes linked by linear monomers. The other one is the connection of two kinds of tetrahedral monomers which could form a **dia-b** net. However, the features of **dia** topology such as flexibility, self-

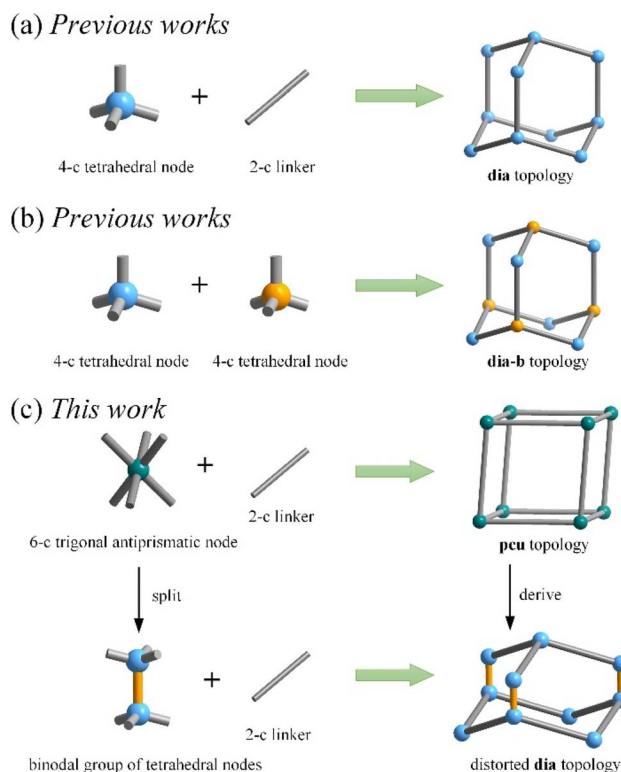


Fig. 1 The routes to achieve **dia** topology COFs. (a) 4-c node and the 2-c linker; (b) 4-c node and the 4-c node; (c) 6-c node and the 2-c linker.

duality, and open framework make it very easy to be interpenetrated (Table S1†). The first Schiff base 3D COF, COF-300 constructed from tetrakis(4-aminophenyl)methane and terephthalaldehyde, was reported as a 5-fold interpenetrated **dia** framework.<sup>52</sup> Its isoreticular-expanded form with linkers having one more phenyl ring, COF-320, was found with a 9-fold **dia** framework.<sup>53</sup> Actually, most of the **dia** COFs are interpenetrated, and the highest interpenetration reaches up to 12-fold.<sup>54</sup> Only a few examples of non-interpenetrated **dia** COFs have been reported, such as PI-COF-4,<sup>55</sup> JUC-550 to -552,<sup>30</sup> and TKCOF-1,<sup>29</sup> CCOF-22-O<sup>n</sup>Pr/CCOF-22-O<sup>n</sup>Bu,<sup>32</sup> and BMTA-TFPM-COF,<sup>56</sup> all of which can be attributed to the steric hindrance around the building units.

Herein, based on the strategy mentioned above, we designed and synthesized an organic monomer with six pendant reactive groups as a 6-coordinated (6-c) building block with a trigonal antiprismatic shape (or distorted octahedral shape). The building block could also be regarded as a binodal group of tetrahedral nodes which also exists in the **dia** net. By the reaction of this building block with linear monomers with different lengths, three isoreticular 3D COFs, JUC-300 to -302, were obtained respectively. The structures of these COFs were determined to be of non-interpenetrated **pcu**-derived **dia** topology (Fig. 1c). The distorted **dia** topology has reduced symmetry and two kinds of edges, and the frameworks were only isoreticular-expanded *via* one of the edges, which could be the reason for avoiding interpenetration.



### Synthesis and characterization of COFs

To synthesize the targeted COFs, we first synthesized the 6-c building unit, 1,4-phenylenebis(tris(4-formylphenyl)silane) (PBTSi-6CHO, Fig. 2a). Synthesis of PBTSi-6CHO was based on a procedure that involved lithium-halogen exchange of the acetal-protected 4-bromobenzaldehyde, followed by its reaction with 1,4-bis(triethoxysilyl)benzene and subsequent deprotection of the aldehyde groups. The geometry of the building unit could be confirmed by the same organosilicon core in the crystal structure of IMP-15.<sup>57</sup> The COFs, JUC-300, -301, and -302, were obtained in good yield by the solvothermal reaction of PBTSi-6CHO with three linear diamines with different lengths which are *p*-phenylenediamine (PPDA), 4,4'-diaminobiphenyl (DABP), or 4,4'-diaminoterphenyl (DATP) respectively (Fig. 2a and b). The Schiff-based reaction was implemented in a mixture of tetrahydrofuran and mesitylene with acetic acid as the catalyst at 120 °C for 3 days.

Fourier transform infrared (FT-IR) spectra of COFs exhibited the depletion of peaks ascribed to NH<sub>2</sub> (~3400 cm<sup>-1</sup>) and C=O (~1690 cm<sup>-1</sup>) stretching vibration and the appearance of characteristic C=N stretching bands at around 1622 cm<sup>-1</sup>,

indicating the successful conversion of aldehyde and amine groups into imine bonds (Fig. S3–S5†). All the solid-state <sup>13</sup>C cross-polarization magic-angle spinning (CP-MAS) NMR spectra for three COFs showed chemical shifts at 158 ppm that match with the C=N resonance which further confirms the formation of imine bonds (Fig. S6–S8†). To determine the composition of COFs, acid-digested <sup>1</sup>H NMR measurements of the washed and activated JUC-300, -301, and -302 were conducted.<sup>58</sup> The <sup>1</sup>H NMR spectra indicated the presence of linkers with a ratio of PBTSi-6CHO to amine linkers to be ~1:3 for all three COFs, which are in accordance with the theoretical values (Fig. S9–S11†).

Thermogravimetric analysis (TGA) under air conditions on activated samples of COFs by acetone exchange and vacuum treatment was conducted. It is demonstrated that there was no significant weight loss up before 200 °C for the three COFs, indicating the exclusion of most of the solvents. There was less than 5% weight loss between 200 and 400 °C for all COFs which could be attributed to the existence of guest molecules with high boiling points which were hardly exhausted by solvent exchange (Fig. S12†). All the COFs exhibited a uniform spherical

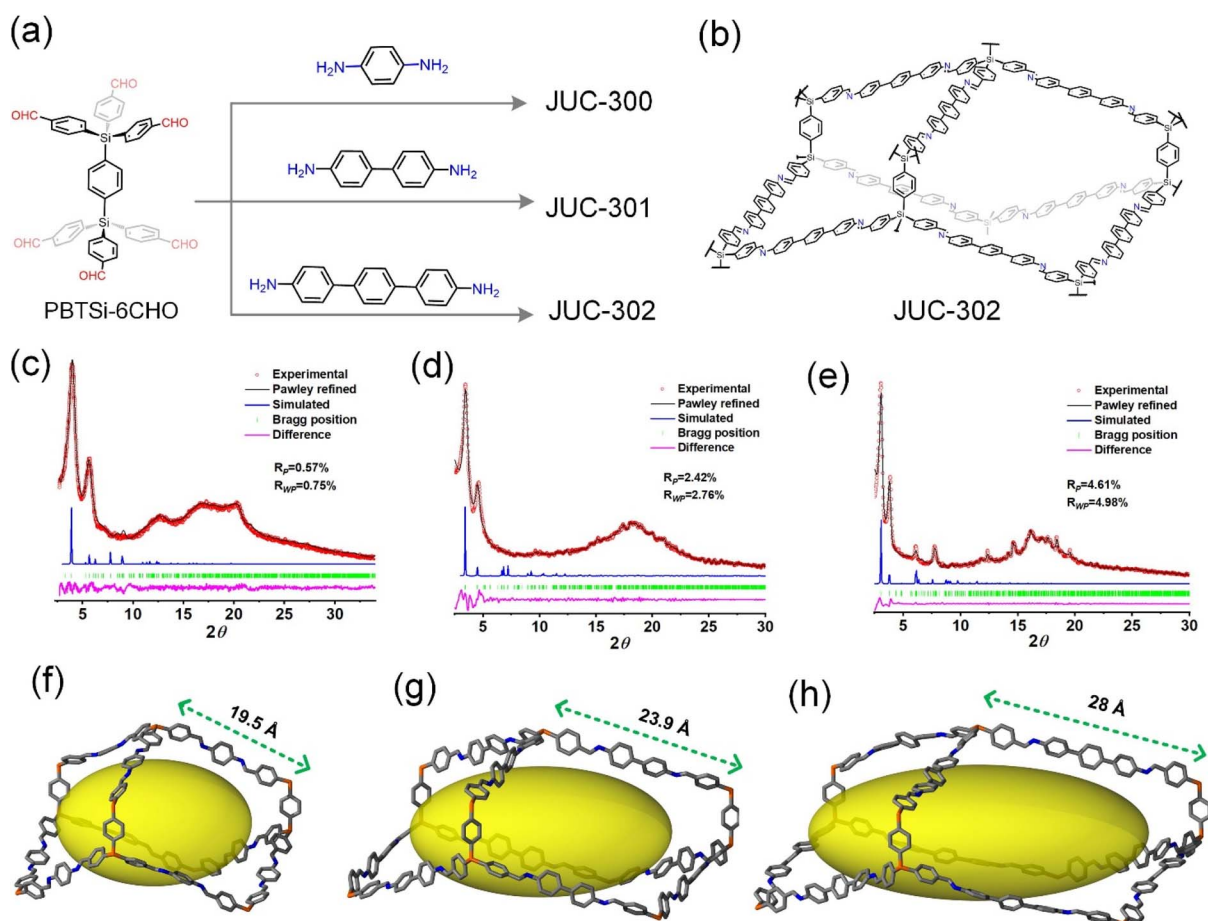


Fig. 2 Synthesis and crystal structures of JUC-300, -301 and -302. (a) Synthesis routes. (b) An adamantane unit of JUC-302. PXRD patterns for JUC-300 (c), JUC-301 (d), and JUC-302 (e): comparison between the experimental (red circle) and Le Bail refined (black) profiles, the simulated patterns for distorted *dia* topology (blue), the Bragg positions (green), and the refinement differences (pink). Pore regulation through isorecticular expansion for JUC-300 (f), -301 (g), and -302 (h) (yellow balls only indicate the free space in an adamantane unit).



morphology, with sizes around 1  $\mu\text{m}$ , composed of intergrown tiny crystals as observed through scanning electron microscopy (SEM, Fig. S13–S15<sup>†</sup>). Transmission electron microscopy (TEM) further revealed that these aggregated crystals were rod-like in shape (Fig. S16–S18<sup>†</sup>), with widths of approximately 20 nm and varying lengths. The length increased in the order of JUC-300, -301, and -302, resulting in the aggregated spheres of JUC-301 and -302 resembling petal-like and leaf-like structures, respectively.

### Structural determination

The structures of COFs were verified by powder X-ray diffraction (PXRD) combined with structural simulations. To construct the structural models of COFs, we first considered the monomer PBTSi-6CHO as a trigonal antiprismatic 6-c node. Given the geometry of PBTSi-6CHO, **pcu** topology was supposed to be the default net of PBTSi-6CHO and linear linkers.<sup>59</sup> Based on the **pcu** net, a distorted **dia** net could be obtained by the splitting of the 6-c node into a binodal group of 4-c tetrahedral nodes (Fig. 1c). Structural models of JUC-300, -301, and -302 were generated based on these **pcu**-derived distorted **dia** nets after energy minimization.

PXRD patterns of JUC-300, -301, and -302 show similar intense peaks but at different  $2\theta$  values (Fig. 2c–e), which indicates that they have similar structures but different dimensions. The positions of the main peaks are getting significantly closer to the low angle in the order of JUC-300, -301, and -302, which is consistent with the increasing length of their linkers. The experimental PXRD patterns of the three COFs fit well with their respective simulated patterns from the structural models. The Le Bail refinements performed using Expo2014 (ref. 60) resulted in good agreement factors for all three COFs ( $R_p = 0.75\%$  and  $R_{w,p} = 0.57\%$  for JUC-300,  $R_p = 8.24\%$  and  $R_{w,p} = 8.13\%$  for JUC-301, and  $R_p = 7.26\%$  and  $R_{w,p} = 7.14\%$  for JUC-302, respectively). All three structural models are in the trigonal space group  $P3_121$  (No. 154). The unit cell parameters optimized after refinements are  $a = b = 31.33 \text{ \AA}$ , and  $c = 41.61 \text{ \AA}$  for JUC-300,  $a = b = 39.32 \text{ \AA}$  and  $c = 39.65 \text{ \AA}$  for JUC-301, and  $a = b = 46.78 \text{ \AA}$  and  $c = 42.07 \text{ \AA}$  for JUC-302, respectively. The identified peaks in experimental PXRD patterns could correspond to the Bragg peaks. The peaks at  $4.0$  and  $5.6^\circ$  for JUC-300 and peaks at  $3.4$  and  $4.6^\circ$  for JUC-301 can be assigned to their (101) and (110) reflections, respectively. The peaks at  $3.0$ ,  $3.8$ ,  $6.0$ , and  $7.7^\circ$  for JUC-302 can be assigned to its (101), (110), (202) and (222) reflections respectively. We also tried alternative structural models for the three 3D COFs with the interpenetrating forms of the same topology, including 2- and 3-fold (Fig. S19–S30<sup>†</sup>), as well as other topologies such as **acs**, **bcs**, **crs** and **lcy** (Fig. S31 and S32<sup>†</sup>). However, the simulated PXRD patterns from these alternatives cannot match the respective experimental ones obviously (Fig. S22, S26, S30 and S32<sup>†</sup>). Thus, the obtained COFs were proposed to have the expected 3D frameworks with non-interpenetrated **pcu**-derived **dia** topology.

As expected, the pore features in the structural models of JUC-300, -301, and -302 are regulated in two dimensions (Fig. 2f–h). Three of the four edges of one tetrahedral node in JUC-300, -301, and -302 structures are elongated to be

approximately 19.5, 23.9, and 28  $\text{\AA}$  respectively, while the fourth edges of one tetrahedral node for the three COFs are all equal to about 6.5  $\text{\AA}$ . Therefore, the pore in their adamantane units was distorted to be ellipsoid, while the pore in classic adamantane units in **dia** topology is a sphere.

### Porosity of COFs

To probe the pore features of the as-synthesized COFs, nitrogen adsorption and desorption measurements at 77 K were conducted. Before the measurements, the samples were activated by acetone exchange and evacuation at 120  $^\circ\text{C}$ . As shown in Fig. 3a, JUC-300 exhibited a typical type I isotherm with a sharp increase at low pressure ( $P/P_0 < 0.05$ ), indicating that it is microporous. The nitrogen adsorption still increased slowly between  $P/P_0 = 0.1$ – $0.9$ , which is common for microporous polymers containing some large pores. Unlike JUC-300, JUC-301 and -302 displayed type IV isotherms with an extra uptake step between  $P/P_0 = 0.4$ – $0.6$  and obvious hysteresis loops which was a typical characteristic of mesoporous materials (Fig. 3d and g). The calculated Brunauer–Emmett–Teller (BET) surface areas of JUC-300, -301, and -302 are 630, 317, and 104  $\text{m}^2 \text{g}^{-1}$  respectively. Pore size distributions (PSDs) for the three COFs were calculated using quenched solid density functional theory (QSDFT). It resulted that the PSD of JUC-300 and -301 showed micropores centered around 1.6 and 2.0 nm respectively, which are approximately similar to the open windows of quasi-cubic pores in their structural models (Fig. 3b and e). The PSD curve of JUC-301 also shows another pore size region centered at 3.7 nm, which could correspond to the diameter of the cavity in its structural model (Fig. 3f, the quasi-cubic cage), whereas JUC-302 only demonstrated its main pore around 5.2 nm, corresponding to the largest cavity in structural mode (Fig. 3i, the quasi-cubic cage). It should be noted that JUC-302 represents the largest pore size among 3D COFs so far (Table S5<sup>†</sup>). Otherwise, we noticed that the surface areas of the three COFs are lower than their expected values. This might be caused by framework transformation, decrystallization of their flexible frameworks, and/or incomplete removal of guests during the activation because of the intrinsic feature of **dia** nets.<sup>61</sup>

To improve the activation of samples for the pore probe, we performed a supercritical carbon dioxide ( $\text{ScCO}_2$ ) treatment before nitrogen sorption measurements. Owing to the low surface tension of  $\text{ScCO}_2$  which could preserve more porosity and delicate structures of porous frameworks, the BET surface areas of  $\text{ScCO}_2$ -activated samples markedly increased, which are 1079, 607, and 250  $\text{m}^2 \text{g}^{-1}$  for JUC-300, -301, and -302 respectively (Fig. S33–S35<sup>†</sup>). The PSD of  $\text{ScCO}_2$ -activated JUC-300 is similar to that of its traditionally activated sample but with increased pore volume, while, for  $\text{ScCO}_2$ -activated JUC-301, the ratio of pore volume between small and large pores also increased compared to its traditionally activated sample. For  $\text{ScCO}_2$ -activated JUC-302, unlike the traditionally activated sample, a small pore around 2.3 nm also comes out which could be attributed to the open windows of the quasi-cubic cage like the other two COFs (Fig. 3h and S35<sup>†</sup>). These results could indicate the effective activation of small pores in COFs by  $\text{ScCO}_2$  treatment. The PSD of  $\text{ScCO}_2$ -



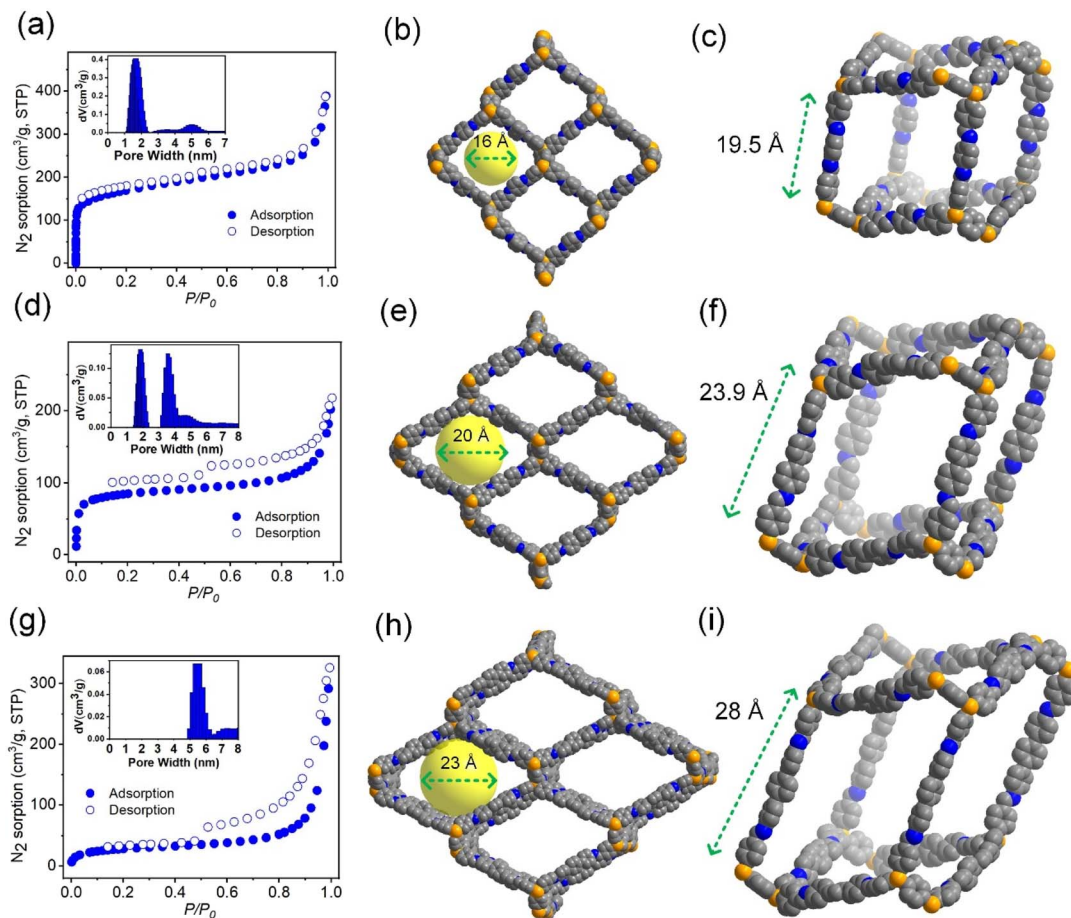


Fig. 3 Porosity of JUC-300, -301 and -302. Nitrogen sorption isotherms at 77 K of JUC-300 (a), -301 (d), and -302 (g) with pore size distributions inserted respectively. Space-filling representation of the structural models of JUC-300 (b and c), -301 (e and f), and -302 (h and i), respectively (gray, C; blue, N; orange, Si; b, e and h, the open windows; c, f and i, the quasi-cubic cages).

activated JUC-302 reveals a more complex array of large pores exceeding 10 nm, likely due to defects forming during the activation processes. This phenomenon also suggests that JUC-302 is the most flexible or fragile among the three of them.

### Flexibility of COFs

To certify the flexibility of COFs, we measured the PXRD patterns of samples with and without solvents. It was found that the crystallinity of JUC-301 and -302 was very easy to lose under ambient conditions, while JUC-300 showed a certain degree of robustness because of its small pores. The diffraction peaks nearly vanished for the as-synthesized samples of JUC-301 and -302 dried in air for more than 10 minutes, while peaks for JUC-300 under the same conditions only diminished slightly. However, only after adding two drops of tetrahydrofuran, the PXRD patterns of JUC-301 and -302 could recover immediately, indicating that their framework changes are dynamic (Fig. 4).

### Protein incorporation

Given that JUC-302 has the largest pore size among 3D COFs and to further define the regulated pores of JUC-300 to -302, we attempted to conduct the incorporation of a protein molecule

with suitable dimensions as the pore probe. The selected protein was myoglobin (Mb,  $M_w = \sim 17$  kDa) with dynamic molecular dimensions of  $2.1 \times 3.5 \times 4.4$  nm<sup>3</sup>.<sup>42,62,63</sup> The activated COFs were immersed in the Mb solution in 0.1 M phosphate buffer solution (PBS, pH = 7.4) with a concentration of 150  $\mu\text{g mL}^{-1}$ . The stability of COFs immersed in PBS was found to be similar to that of the COFs dried in air. PXRD patterns of JUC-301 and -302 showed no diffraction peaks when the samples were dried after immersion in PBS. Nonetheless, the peaks could be recovered after adding two drops of tetrahydrofuran (Fig. S36 and S37<sup>†</sup>). This result could be repeated for at least two cycles. FT-IR spectra also showed no significant changes in the characteristic  $-\text{C}=\text{N}-$  bonds, suggesting that the imine linkages are chemically stable in PBS for Mb adsorption (Fig. S38<sup>†</sup>).

The uptake ability of COFs for Mb was estimated using the amount of Mb remaining in suspension which was monitored by its characteristic absorbance at 409 nm in the UV-vis spectrum over a period of 36 hours (Fig. S39 and S40<sup>†</sup>). As shown in Fig. 5a, the Mb solution with JUC-300 shows a minimal decrease of UV-vis absorbance (only 10% after 36 hours), indicating that there was a small amount of Mb adsorbed by JUC-300. This result agreed with the small pore



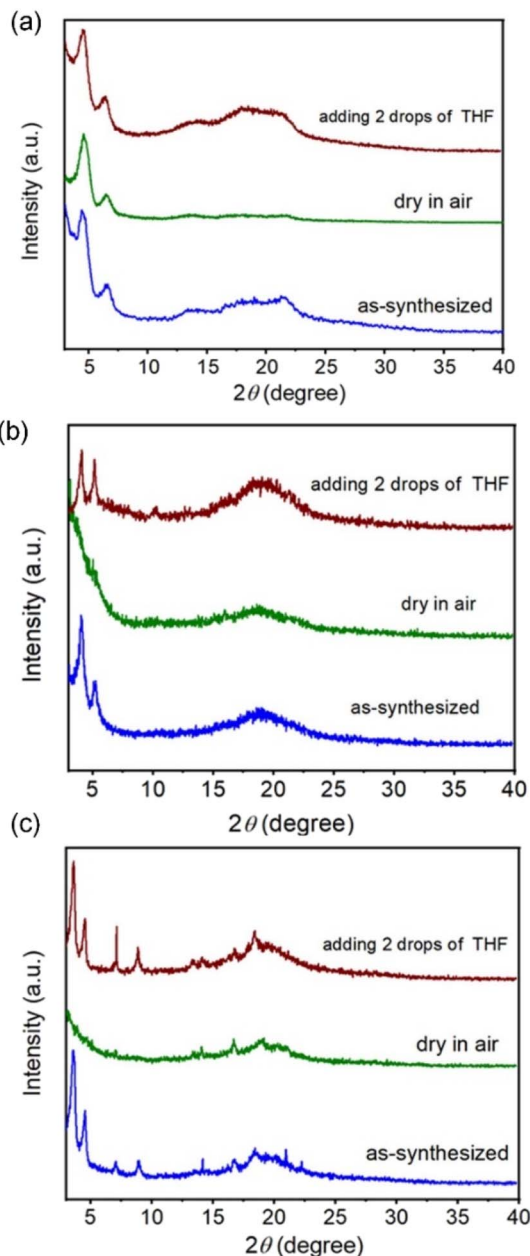


Fig. 4 Flexibility of COFs. PXRD patterns of JUC-300 (a), JUC-301 (b), and JUC-302 (c) with and without solvents.

size of JUC-300 although it has the largest BET surface area among the three COFs. The decrease in UV-vis absorbance for Mb solution with JUC-301 was demonstrated to be 21% after 36 hours, while JUC-302 shows the largest decrease which reaches 52.7% after 36 hours (Fig. 5b and c). The estimated values of adsorbed Mb by JUC-300, -301, and 302 after 36 hours are 38, 79, and 197  $\text{mg g}^{-1}$  respectively (Fig. 5d). Thus, the Mb adsorption capacities of the three COFs are in reverse order of their BET surface areas but in the same order of their pore sizes, indicating the importance of pore size for adsorption and their successful pore regulation. The much higher Mb adsorption capacity of JUC-302 further validates its large pore

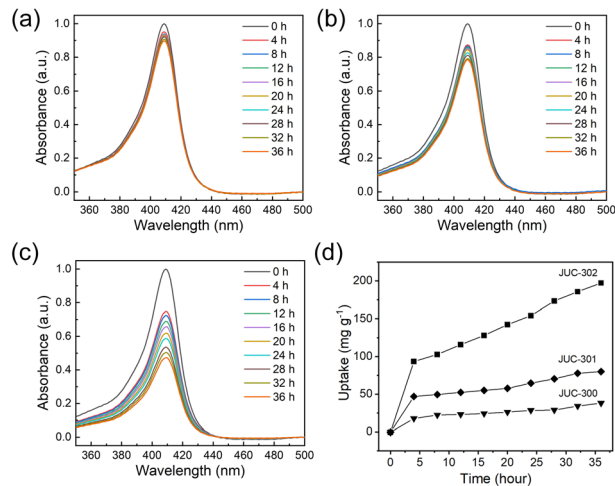


Fig. 5 Protein incorporation by COFs. (a–c) UV-vis absorption spectra of Mb solution with JUC-300 (a), -301 (b), and -302 (c), respectively, at different time points. For each measurement, the initial absorbance was normalized to 1.0. (d) Profiles of Mb uptakes by JUC-300 (triangle), -301 (rhombus), and -302 (square) over a period of 36 hours.

size and positions it as an exceptionally promising candidate for the encapsulation of macromolecular proteins.

## Conclusions

In conclusion, we reported a novel strategy to construct isoreticular 3D COFs with regulated pore sizes by avoiding interpenetration, which is the utilization of high-coordinated building blocks with multi-nodal units. Based on this strategy, three isoreticular-expanded COFs, JUC-300, -301, and -302 with non-interpenetrated **pcu**-derived **dia** topology, were synthesized by using 6-c PBTSi-6CHO with a trigonal antiprismatic shape and three linear diamines with different lengths respectively. Their apparent pore sizes were demonstrated from micropores around 1.6 nm for JUC-300 to mesopores around 5.2 nm for JUC-302. Moreover, the largest pore of JUC-302 among 3D COFs so far endows it with high adsorption capacity for protein Mb although its surface area is the lowest among the three of them. This work not only presents three new flexible isoreticular COFs with regulated pore sizes, but also provides a new pathway for the reticular synthesis of crystalline porous frameworks with reduced interpenetration.

## Data availability

All relevant data are presented in the main text and ESI.†

## Author contributions

X. L. and F. S. conceived and designed the experiments. X. L. and T. Z. prepared the COFs and measured the adsorption. F. Z., Y. S. and H. R. helped analyse the data. X. L., W. W., H. R., and F. S. drafted and revised the manuscript. All authors discussed the results and reviewed the manuscript.



## Conflicts of interest

There are no conflicts to declare.

## Acknowledgements

This research work was supported by the National Natural Science Foundation of China (21871105), the Foundation of Science and Technology Development of Jilin Province, China (20240101174JC), and the National Natural Science Foundation of China (21975096 and 21501064).

## Notes and references

- C. S. Diercks and O. M. Yaghi, *Science*, 2017, **355**, eaal1585.
- A. P. Cote, A. I. Benin, N. W. Ockwig, M. O'Keeffe, A. J. Matzger and O. M. Yaghi, *Science*, 2005, **310**, 1166–1170.
- Y. Xie, W. Wang, Z. Zhang, J. Li, B. Gui, J. Sun, D. Yuan and C. Wang, *Nat. Commun.*, 2024, **15**, 3008.
- Z. Z. Tang, J. Chen, Y. L. Xu, Z. L. Li, L. Sheng, Y. Hu, X. L. Wang, J. L. Wang, Y. P. Tang, X. M. He and H. Xu, *Chem. Mater.*, 2024, **36**, 4437–4443.
- S. Y. Ding, J. Gao, Q. Wang, Y. Zhang, W. G. Song, C. Y. Su and W. Wang, *J. Am. Chem. Soc.*, 2011, **133**, 19816–19822.
- R. F. Chen, Y. Wang, Y. Ma, A. Mal, X. Y. Gao, L. Gao, L. J. Qiao, X. B. Li, L. Z. Wu and C. Wang, *Nat. Commun.*, 2021, **12**, 1354.
- L. Wei, T. Sun, Z. L. Shi, Z. Z. Xu, W. Wen, S. Jiang, Y. B. Zhao, Y. H. Ma and Y. B. Zhang, *Nat. Commun.*, 2022, **13**, 7936.
- C.-R. Zhang, W.-R. Cui, S.-M. Yi, C.-P. Niu, R.-P. Liang, J.-X. Qi, X.-J. Chen, W. Jiang, X. Liu, Q.-X. Luo and J.-D. Qiu, *Nat. Commun.*, 2022, **13**, 7621.
- D. L. Jiang, *Chem*, 2020, **6**, 2461–2483.
- H. M. El Kaderi, J. R. Hunt, J. L. Mendoza Cortes, A. P. Cote, R. E. Taylor, M. O'Keeffe and O. M. Yaghi, *Science*, 2007, **316**, 268–272.
- B. Gui, G. Q. Lin, H. M. Ding, C. Gao, A. Mal and C. Wang, *Acc. Chem. Res.*, 2020, **53**, 2225–2234.
- Q. Zhu, X. Wang, R. Clowes, P. Cui, L. J. Chen, M. A. Little and A. I. Cooper, *J. Am. Chem. Soc.*, 2020, **142**, 16842–16848.
- X. X. Wang, Y. C. Jin, N. Li, H. Zhang, X. L. Liu, X. Y. Yang, H. H. Pan, T. Y. Wang, K. Wang, D. D. Qi and J. Z. Jiang, *Angew. Chem., Int. Ed.*, 2024, **63**, e202401014.
- G. Y. Qiao, X. X. Wang, X. Li, J. Li, K. Y. Geng, E. Q. Jin, J. J. Xu and J. H. Yu, *J. Am. Chem. Soc.*, 2024, **146**, 3373–3382.
- Y. K. Liu, X. A. Liu, A. Su, C. T. Gong, S. W. Chen, L. W. Xia, C. W. Zhang, X. H. Tao, Y. Li, Y. H. Li, T. L. Sun, M. R. Bu, W. Shao, J. Zhao, X. N. Li, Y. W. Peng, P. Guo, Y. Han and Y. H. Zhu, *Chem. Soc. Rev.*, 2024, **53**, 502–544.
- J. Li, C. Lin, T. Ma and J. Sun, *Nat. Commun.*, 2022, **13**, 4016.
- Y. Lan, X. Han, M. Tong, H. Huang, Q. Yang, D. Liu, X. Zhao and C. Zhong, *Nat. Commun.*, 2018, **9**, 5274.
- R. Freund, S. Canossa, S. M. Cohen, W. Yan, H. X. Deng, V. Guillerm, M. Eddaoudi, D. G. Madden, D. Fairen-Jimenez, H. Lyu, L. K. Macreadie, Z. Ji, Y. Y. Zhang, B. Wang, F. Haase, C. Wöll, O. Zaremba, J. Andreo, S. Wuttke and C. S. Diercks, *Angew. Chem., Int. Ed.*, 2021, **60**, 23946–23974.
- G. L. Hu, Q. Liu, Y. Zhou, W. Yan, Y. Q. Sun, S. Peng, C. B. Zhao, X. Zhou and H. X. Deng, *J. Am. Chem. Soc.*, 2023, **145**, 13181–13194.
- H. X. Deng, S. Grunder, K. E. Cordova, C. Valente, H. Furukawa, M. Hmadeh, F. Gandara, A. C. Whalley, Z. Liu, S. Asahina, H. Kazumori, M. O'Keeffe, O. Terasaki, J. F. Stoddart and O. M. Yaghi, *Science*, 2012, **336**, 1018–1023.
- L. F. Song, J. Zhang, L. X. Sun, F. Xu, F. Li, H. Z. Zhang, X. L. Si, C. L. Jiao, Z. B. Li, S. Liu, Y. L. Liu, H. Y. Zhou, D. L. Sun, Y. Du, Z. Cao and Z. Gabelica, *Energy Environ. Sci.*, 2012, **5**, 7508–7520.
- M. Eddaoudi, J. Kim, N. Rosi, D. Vodak, J. Wachter, M. O'Keeffe and O. M. Yaghi, *Science*, 2002, **295**, 469–472.
- M. Martinez-Abadia, K. Strutynski, B. Lerma-Berlanga, C. T. Stoppioello, A. N. Khlobystov, C. Marti-Gastaldo, A. Saeki, M. Melle-Franco and A. Mateo-Alonso, *Angew. Chem., Int. Ed.*, 2021, **60**, 9941–9946.
- R. M. Zhu, J. W. Ding, L. Jin and H. Pang, *Coord. Chem. Rev.*, 2019, **389**, 119–140.
- H.-L. Jiang, T. A. Makal and H.-C. Zhou, *Coord. Chem. Rev.*, 2013, **257**, 2232–2249.
- G. Verma, S. Butikofer, S. Kumar and S. Q. Ma, *Top. Curr. Chem.*, 2019, **378**, 4.
- T. Ma, J. Li, J. Niu, L. Zhang, A. S. Etman, C. Lin, D. Shi, P. Chen, L. H. Li, X. Du, J. Sun and W. Wang, *J. Am. Chem. Soc.*, 2018, **140**, 6763–6766.
- Y. Z. Liu, Y. H. Ma, J. J. Yang, C. S. Diercks, N. Tamura, F. Y. Jin and O. M. Yaghi, *J. Am. Chem. Soc.*, 2018, **140**, 16015–16019.
- X. H. Wang, Y. Wada, T. Shimada, A. Kosaka, K. Adachi, D. Hashizume, K. Yazawa, H. Uekusa, Y. Shoji, T. Fukushima, M. Kawano and Y. Murakami, *J. Am. Chem. Soc.*, 2024, **146**, 1832–1838.
- Y. J. Wang, Y. Z. Liu, H. Li, X. Y. Guan, M. Xue, Y. S. Yan, V. Valchev, S. L. Qiu and Q. R. Fang, *J. Am. Chem. Soc.*, 2020, **142**, 3736–3741.
- L. Liao, X. Guan, H. Zheng, Z. Zhang, Y. Liu, H. Li, L. Zhu, S. Qiu, X. Yao and Q. Fang, *Chem. Sci.*, 2022, **13**, 9305–9309.
- K. X. Wang, B. Hou, J. Q. Dong, H. L. Niu, Y. Liu and Y. Cui, *J. Am. Chem. Soc.*, 2024, **146**, 21466–21475.
- Y. Ma, J. Li, D. Sun, Y. Wu, C. Liu and H. Li, *ACS Appl. Mater. Interfaces*, 2024, **16**, 45383–45388.
- A. Schoedel, M. Li, D. Li, M. O'Keeffe and O. M. Yaghi, *Chem. Rev.*, 2016, **116**, 12466–12535.
- R. R. Liang, S. Y. Jiang, R. H. A and X. Zhao, *Chem. Soc. Rev.*, 2020, **49**, 3920–3951.
- L. X. Li, Q. B. Yun, C. Z. Zhu, G. Sheng, J. Guo, B. Chen, M. T. Zhao, Z. C. Zhang, Z. C. Lai, X. Zhang, Y. W. Peng, Y. H. Zhu and H. Zhang, *J. Am. Chem. Soc.*, 2022, **144**, 6475–6482.
- Z. J. Mu, Y. H. Zhu, B. X. Li, A. W. Dong, B. Wang and X. Feng, *J. Am. Chem. Soc.*, 2022, **144**, 5145–5154.
- P. Li, Q. S. Chen, T. C. Wang, N. A. Vermeulen, B. L. Mehdi, A. Dohnalkoya, N. D. Browning, D. K. Shen, R. Anderson,



- D. A. Gómez-Gualdrón, F. M. Cetin, J. Jagiello, A. M. Asiri, J. F. Stoddart and O. K. Farhal, *Chem*, 2018, **4**, 1022–1034.
- 39 J. T. Li, D. F. Sava, V. Guillermin, T. Melliti, R. Luebke, J. F. Eubank, P. M. Bhatt, H. Jiang, M. Bonneau, Y. Belmabkhout, Z. Y. Huang, A. Shkurenko, L. Wojtas, M. O’Keeffe and M. Eddaoudi, *Chem*, 2024, **10**, 567–577.
- 40 H. Jiang, S. M. Moosavi, J. Czaban-Jozwiak, B. Torre, A. Shkurenko, Z. O. Ameer, J. T. Jia, N. Alsadun, O. Shekhah, E. Di Fabrizio, B. Smit and M. Eddaoudi, *Matter*, 2023, **6**, 285–295.
- 41 N. Arora, C. Flores, M. C. Senarathna, C. M. Thompson and R. A. Smaldone, *CCS Chem.*, 2024, **6**, 57–68.
- 42 H. Li, J. H. Ding, X. Y. Guan, F. Q. Chen, C. Y. Li, L. K. Zhu, M. Xue, D. Q. Yuan, V. Valtchev, Y. S. Yan, S. L. Qiu and Q. R. Fang, *J. Am. Chem. Soc.*, 2020, **142**, 13334–13338.
- 43 Y. C. Wang, C. Y. Wu, W. J. Sun, Q. Y. Pan, W. B. Hao, H. Liu, J. Sun, Z. B. Li, J. L. Sun and Y. J. Zhao, *Mater. Chem. Front.*, 2021, **5**, 944–949.
- 44 H. Y. Liu, Y. Zhou, J. B. Guo, R. Feng, G. L. Hu, J. D. Pang, Y. Chen, O. Terasaki and X. H. Bu, *J. Am. Chem. Soc.*, 2023, **145**, 23227–23237.
- 45 Y. Zhao, S. Das, T. Sekine, H. Mabuchi, T. Irie, J. Sakai, D. Wen, W. D. Zhu, T. Ben and Y. Negishi, *Angew. Chem., Int. Ed.*, 2023, **62**, e202300172.
- 46 L. A. Baldwin, J. W. Crowe, D. A. Pyles and P. L. McGrier, *J. Am. Chem. Soc.*, 2016, **138**, 15134–15137.
- 47 Z. L. Li, C. H. Hsueh, Z. Z. Tang, J. Chen, X. L. Wang, H. Cui, Y. Yang, X. D. Wang, D. S. Ren, H. Q. Gao, M. Y. Li, H. Xu and X. M. He, *SusMat*, 2022, **2**, 197–205.
- 48 D. Y. Zhu, Y. F. Zhu, Y. Chen, Q. Q. Yan, H. Wu, C. Y. Liu, X. Wang, L. B. Alemany, G. H. Gao, T. P. Senftle, Y. Peng, X. Wu and R. Verduzco, *Nat. Commun.*, 2023, **14**, 2865.
- 49 X. Y. Guan, Y. C. Ma, H. Li, Y. Yusran, M. Xue, Q. R. Fang, Y. S. Yan, V. Valtchev and S. L. Qiu, *J. Am. Chem. Soc.*, 2018, **140**, 4494–4498.
- 50 F. Z. Jin, E. Lin, T. H. Wang, S. B. Geng, T. Wang, W. S. Liu, F. H. Xiong, Z. F. Wang, Y. Chen, P. Cheng and Z. J. Zhang, *J. Am. Chem. Soc.*, 2022, **144**, 5643–5652.
- 51 T. T. Ma, G. Z. Huang, X. H. Wang, Y. Liang, R. H. Li, B. Wang, S. J. Yao, J. P. Liao, S. L. Li, Y. Yan and Y. Q. Lan, *Natl. Sci. Rev.*, 2024, **11**, nwa177.
- 52 F. J. Uribe-Romo, J. R. Hunt, H. Furukawa, C. Klock, M. O’Keeffe and O. M. Yaghi, *J. Am. Chem. Soc.*, 2009, **131**, 4570–4571.
- 53 Y. B. Zhang, J. Su, H. Furukawa, Y. F. Yun, F. Gándara, A. Duong, X. D. Zou and O. M. Yaghi, *J. Am. Chem. Soc.*, 2013, **135**, 16336–16339.
- 54 B. Gui, J. J. Xin, Y. P. Cheng, Y. F. Zhang, G. Q. Lin, P. H. Chen, J. X. Ma, X. Zhou, J. L. Sun and C. Wang, *J. Am. Chem. Soc.*, 2023, **145**, 11276–11281.
- 55 Q. R. Fang, J. H. Wang, S. Gu, R. B. Kaspar, Z. B. Zhuang, J. Zheng, H. X. Guo, S. L. Qiu and Y. S. Yan, *J. Am. Chem. Soc.*, 2015, **137**, 8352–8355.
- 56 M. H. Liu, H. Y. Kong, S. Bi, X. S. Ding, G. Z. Chen, J. He, Q. Xu, B. H. Han and G. F. Zeng, *Adv. Funct. Mater.*, 2023, **33**, 2302637.
- 57 R. P. Davies, P. D. Lickiss, K. Robertson and A. J. P. White, *CrystEngComm*, 2012, **14**, 758–760.
- 58 B. Zhang, H. Y. Mao, R. Matheu, J. A. Reimer, S. A. Alshimri, S. Alshihri and O. M. Yaghi, *J. Am. Chem. Soc.*, 2019, **141**, 11420–11424.
- 59 N. W. Ockwig, O. Delgado Friedrichs, M. O’Keeffe and O. M. Yaghi, *Acc. Chem. Res.*, 2005, **38**, 176–182.
- 60 A. Altomare, C. Cuocci, C. Giacobozzo, A. Moliterni, R. Rizzi, N. Corriero and A. Falcicchio, *J. Appl. Crystallogr.*, 2013, **46**, 1231–1235.
- 61 C. Q. Ji, C. J. Kang, B. C. Patra and D. Zhao, *CCS Chem.*, 2024, **6**, 856–881.
- 62 T. A. Wang, I. F. Azhar, Y. T. Yang, Y. Lu, Y. Y. Tian, N. Gao, F. C. Cui, L. Yang, X. F. Jing and G. S. Zhu, *Nano Res.*, 2022, **15**, 4569–4574.
- 63 R.-T. Gao, S.-Y. Li, Y. Zong, Z. Chen, N. Liu and Z.-Q. Wu, *Angew. Chem., Int. Ed.*, 2024, **63**, e202410010.

